INL/JOU-20-58300-Revision-0

Microstructure evolution of U-Zr system in a thermal cycling neutron diffraction experiment : I. Extruded U-10Zr (wt. %)

February 2021

Yi Xie, Sven C. Vogel, Jason M. Harp, Michael T Benson, Luca Capriotti

Changing the World's Energy Future

INL is a U.S. Department of Energy National Laboratory operated by Battelle Energy Alliance, LLC

INL/JOU-20-58300-Revision-0

Microstructure evolution of U-Zr system in a thermal cycling neutron diffraction experiment : I. Extruded U-10Zr (wt. %)

Yi Xie, Sven C. Vogel, Jason M. Harp, Michael T Benson, Luca Capriotti

February 2021

Idaho National Laboratory
Idaho Falls, Idaho 83415

http://www.inl.gov

Prepared for the
U.S. Department of Energy
Under DOE Idaho Operations Office
Contract DE-AC07-05ID14517, DE-AC07-05ID14517

Microstructure Evolution of U–Zr System in A Thermal Cycling Neutron Diffraction Experiment: I. Extruded U–10Zr (wt. %)

Yi Xie[1,2]*, Sven C. Vogel[3], Jason M. Harp[4,5], Michael T. Benson[1], Luca Capriotti[4]

[1]Advanced Fuel Manufacturing and Development Department, Idaho National Laboratory, Idaho Falls, ID 83415, USA

[2]School of Nuclear Engineering, Purdue University, West Lafayette, IN 47906, USA

[3]Material Science and Technology Division, Los Alamos National Laboratory, Los Alamos, NM 87545, USA

[4]Post Irradiation Examinations Department, Idaho National Laboratory, Idaho Falls, ID 83415, USA

[5]Reactor and Nuclear Systems Division, Oak Ridge National Laboratory, Oak Ridge, TN 37831, USA

Abstract

Microstructure evolution of 800°C extruded U–10Zr (wt. %) fuel during thermal cycling (30–800°C with a ~9 hour hold at 600°C during cooling) was investigated using in situ neutron diffraction. Analysis was performed using Rietveld texture and crystal structure refinements from time–of–flight neutron diffraction data, with a focus on the evolution of textures and lattice parameters as a function of temperature. The α–U phase exhibits lattice contraction with increasing temperature along the *b* lattice direction and lattice expansion in the other directions while the other phases exhibit lattice expansion with temperature in all directions. Contrary to the established phase diagram, the β–U phase is absent at the temperatures of the thermal cycling. $(001)_{\alpha}$ and $(110)_{\gamma}$ plane normals are observed with a strong preferred orientation along the extrusion direction. The variant selection of $(001)_{\alpha}||(110)_{\gamma}$ is observed for the first time.

Keywords: U–10Zr; Extrusion; In–situ high temperature neutron diffraction; Texture; Lattice parameter

*Corresponding author: xie90@purdue.edu

1. Introduction

U–Zr–based nuclear fuel is a leading choice for sodium–cooled fast reactors, as it has advantages of high fissile density, high thermal conductivity, ease of fabrication, and good compatibility with coolants [1] [2] [3]. The U–Zr system is also the basis for transmutation fuels, allowing to burnup fission products from spent fuels such as Pu, Np, Am [4] [5] [6]. The Zr present in U–Zr increases the solidus/liquidus temperatures relative to pure uranium and imparts resistance to fuel–cladding chemical interaction. U–Zr fuel is anticipated to be fabricated in rod geometry, which can be produced by different processes, including injection casting [7] and extrusion [8]. Understanding the dimensional changes and evolution of the microstructure, in particular phase composition and texture, as a result of irradiation and thermal cycling at elevated temperatures, is of paramount importance for the development and ultimately licensing of this fuel form.

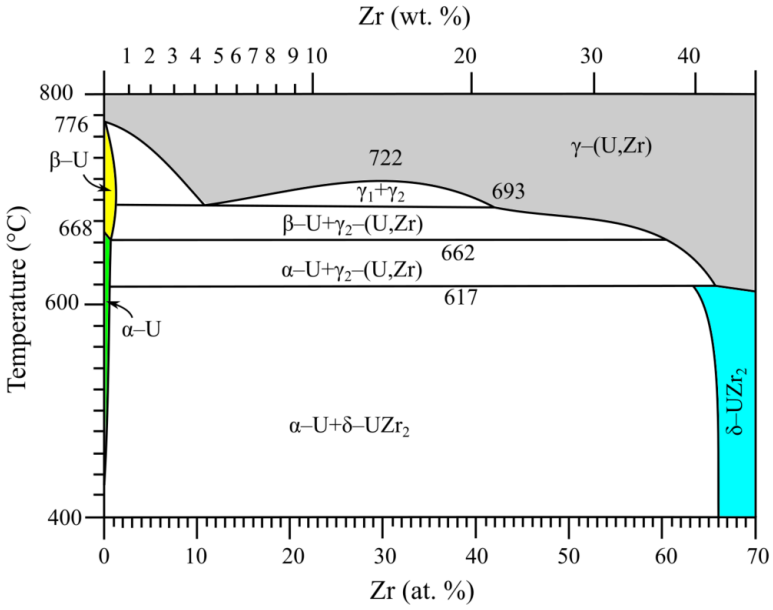

Figure 1. U-rich portion of the U–Zr phase diagram from Ref. [9]. U–10Zr (wt. %) is equivalent to U–23Zr (at. %).

The widely accepted equilibrium phase diagram of U–Zr is given in Ref. [9] and the U-rich portion is shown in Figure 1. The U–Zr system contains four stable U–bearing phases (see [1] for detailed discussion of the crystal structures), which are the high–temperature phases γ–(U,Zr) (body centered cubic [BCC]) and β–U (tetragonal), as well as the low–temperature phases α–U (orthorhombic) and δ–UZr_2 (hexagonal). γ–(U,Zr) is the solid solution between γ–U and β–Zr, stable in all concentrations and separating into two BCC solid solutions (γ_1 and γ_2) at temperatures below 722°C. The solidus temperature

of γ–(U,Zr) increases with increasing Zr concentration from 1135°C (melting point of U) to 1855°C (melting point of Zr). For U–10Zr fuel, the solidus temperature is 1220°C, which is higher than the melting temperature of pure U, 1135°C, thus providing an operational safety benefit for U–Zr over pure U. The γ–(U,Zr), due to its cubic crystal structure, exhibits isotropic thermal expansion and isotropic thermal conductivity. The α–U phase has anisotropic coefficients of thermal expansion for its crystal directions, with the linear expansion at different temperatures in the *a* and *c* directions about 0.3% — 2.3% and 0.2% — 2.1%, respectively, while in the *b* direction it is about -0.002% — -0.05% [10]. Deformation behavior of α–U is complex [11], as four slip modes and at least three twinning modes are accounted for the deformation mechanism [12][13]. The behavior of U–10Zr alloy fuel under irradiation is impacted by the presence of all these phases that occur over the temperature gradient present in fuel for fast reactors operated under typical conditions. The outer radius of the fuel typically operates between 500 and 600°C, leaving a ring of fuel in the U–10Zr case in the α–U phase. Depending on operating conditions and geometry, there may be a portion of the fuel above the α–β phase transformation temperature (667°C) and a portion of the fuel fully in the γ phase (>693°C). The mobility of Zr is less in α–U than in β–U, while the maximum concentration of Zr in the α and β phase is less than a few atom percent (see [1] and references therein for a detailed discussion of the phases occurring in the U–Zr system). However, Zr is fully miscible in the γ–(U,Zr) phase, therefore β–U is expected based on the phase diagram in the intermediate radius of the fuel as the Zr atoms are migrating towards the center radius, forming γ–(U,Zr). This phenomenon is known as constituent redistribution [14].

The U–10Zr fuel exhibits swelling asymmetry during irradiation, as it contains anisotropic orthorhombic and hexagonal crystal structures. The strong anisotropy of these non–cubic crystal symmetry phases results in anisotropic fuel swelling. In conjunction with the fabrication induced preferred orientation, such as hot extrusion, this leads to anisotropic swelling in the bulk fuel. Geometric change and deformation may be created by metal forming processes and needs to be carefully understood and controlled. A previous study on the 600°C extruded (in the [α+δ] region) U–10Zr fuel found a strong texture with the α–(100) poles aligned parallel to the extrusion direction [15]. A higher extrusion temperature in the γ phase region is desired to make the fuel easier to deform [8]. However, a systematic investigation of hot extruded fuels in the high temperature γ phase region has not been performed.

The crystallographic texture of non–cubic crystal structures will affect bulk thermal expansion of fuel alloys arising from the significant anisotropy of thermal expansion at the crystallographic level. Detailed understanding of how the crystallographic textures evolve in relation to processing or operating temperature is of great importance for evaluating anisotropic swelling and optimizing fabrication routes. Most studies of crystallographic texture in U–Zr alloys have focused on measurements of low–temperature phases (e.g. [13][16]). This is because conventional techniques of texture analysis (e.g.,

X–ray diffraction and electron backscatter diffraction) can usually operate only at ambient temperature. Investigations of high temperature phases β and γ are lacking as measuring these textures at high temperature or quenching high temperature phases to room temperature is experimentally challenging. Neutron diffraction enables such in situ studies.

The study described herein investigated the evolution of texture and lattice parameters during thermal cycling and explored changes in preferred orientation patterns through the phase transformations carried out in U–10Zr. The U–10Zr alloy was hot–extruded at 800°C before neutron diffraction. In order to achieve an effective control of phase–relevant effects (e.g., fission gas swelling, constituent redistribution) to develop this fuel form, a detailed understanding of the microstructural changes during phase transformations is needed. Neutron diffraction, which uses penetrating radiation, has been demonstrated to be a powerful technique for the measurement of bulk textures under nonambient conditions, especially for materials that oxidize in air (e.g., [15][17]).

2. Material and Methods

2.1. Material

Uranium and Zr were initially cast into an alloy in an arc-melter within an argon atmosphere glovebox (less than 10 ppm oxygen and 10 ppm water) with high purity argon as cover gas. After adding the appropriate amount of each element in its pure metallic form, the alloy was cast into a button, and flipped and re–melted at least three times to ensure homogeneity. The U–10Zr alloy was cast into a billet 36.8 mm in diameter followed by hot extrusion at a preheating temperature of 800°C into a pin of 11.4 mm in diameter. Zr cladding, comprised of pure Zr (ASTM grade 702), was co–extruded along with the U–10Zr alloy. Details of the extrusion process are presented by Pace and Mackowiak [8]. Approximately 10 mm of length was cut from each pin for the neutron diffraction experiments.

2.2. In–situ heating neutron diffraction

In–situ heating neutron diffraction was performed on the time–of–flight high–pressure–preferred orientation (HIPPO) diffractometer [18] at the pulsed spallation neutron source at the Los Alamos Neutron Science Center (LANSCE). To collect the diffraction patterns under a ~10^{-6} Torr vacuum at high temperatures, a resistive furnace made of vanadium heating elements and heat shields was used. The sample was held in vanadium sample holders, an element with negligible contribution to the diffraction pattern and compatible with U–Zr alloys. The instrument provides a large angular detector coverage of ~22.4% of 4π [19] with its detector banks at nominal diffraction angles of 140°, 120°, 90°, 60°, and 40°. The large coverage in conjunction with the comparably short distance of ~8.9 m between neutron moderator and sample provides very high neutron count rates, optimizing data collection time. The sample was rotated three times around its vertical axis at –45°, 22.5°, and 45° to allow for texture

measurements or randomized crystal orientations when integrating data from all detector panels and rotations, allowing for analysis assuming random powders with improved counting statistics.

The temperature was recorded by two thermocouples (one to control the furnace temperature, a second one as an alarm thermocouple) located within the hot zone of the furnace. The deviation between the two thermocouples was less than 2°C. The temperature reading, corresponding to the average of the two thermocouple measurements, is shown in Figure 2. The annealing cycle started at 30°C. Using a ramp rate of 1°C/min, the sample was heated to 200°C. Using a ramp rate of 20°C/min for higher temperature changes, the sample was heated to 600°C and 650°C, followed by 5°C increments from 650 to 700°C with ~16 minutes hold time at each of these temperatures and a dwell of 16 minutes at the maximum temperature of 800°C. The same profile was repeated during cooling except that the microstructure evolution at 600°C was followed for ~540 min. At each dwell point, neutron data was collected for a proton current corresponding to 1–2 minutes per sample rotation or 5 minutes total at a proton linear accelerator current of 100 μA, thus compensating for fluctuations in proton current and providing datasets of approximately constant total neutrons counts.

Measurements were longer at 200°C than other temperatures. From 600°C heating to 800°C and to 650°C cooling, samples were repeatedly measured three times at each rotation, with an exposure time of roughly 2 minutes for each measurement. Accordingly, the three repeats occurred at 0–5 minutes, 6–11 minutes, and 11–16 minutes, separately. At other temperatures, the measurement time was longer than 16 minutes. Temperatures were selected to investigate the low– and high–temperature phases and phase transformations and their kinetics based on the U–Zr binary phase diagram (see Figure 1). In principle, low–temperature phases transform to high–temperature phases during heating and return to the low–temperature phases during cooling. Diffraction patterns were collected to observe the evolution of texture and lattice parameters during phase transformation and thermal expansion.

For the hot extruded U–10Zr, crystal structures and textures were analyzed from the diffraction patterns using the Rietveld software Material Analysis Using Diffraction (MAUD) with the E–WIMV algorithm (15° resolution) following procedures described by Wenk et al. [20]. The crystal structures and volume fractions were refined with both MAUD and the General Structure Analysis System (GSAS) [21] automated with scripts in gsaslanguage [22]. The results agreed mostly within error bars, with significant differences explained by differences in the Rietveld model such as different descriptions of the background. Refinements started with the data collected at room temperature using the α–U lattice parameters as an internal standard as this phase is not subject to lattice parameter variations due to variations in alloy composition. This refinement along with parameters were used as starting parameters to refine the patterns at higher temperatures, with the DIFC parameters fixed [20] [21], thus essentially recalibrating the original sample position and therefore providing reliable absolute lattice parameters at

higher temperatures. Refined parameters included the *y* atomic position in α–U, lattice parameters, weight fractions of all phases and an isotropic thermal motion parameter U_{iso}. To ensure numerical stability of the refinement procedure, the U_{iso} parameter was constrained to be identical for all phases as this parameter may otherwise lead to unphysical values especially for small phase fractions. This leads to systematic deviations in the weight fractions of the phases on the order of a few percent, see below for the discussion of the weight fraction of the Zr cladding that should be constant.

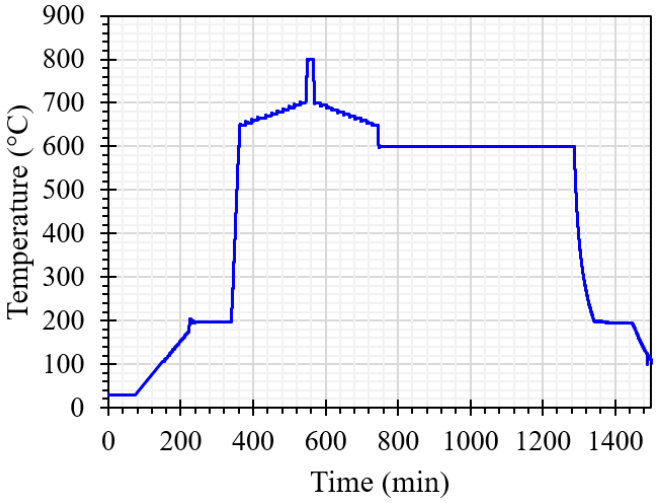

Figure 2. Measured temperature as a function of time. On heating, the sample temperature starts at 30°C, increases to 200°C with a ramp rate of 1°C/min, followed by 600, 650, 655, …, 695, 700, and 800°C with a ramp rate of 20°C/min. Between 650 and 700°C, the temperature was changed in increments of 5°C every ~16 minutes during heating and cooling. On cooling, the temperature was held at 600°C for 540 minutes before decreasing back to 200°C.

3. Results

3.1. Overall diffraction results

Figure 3 shows a section from 1.2–3.0 Å in d–spacing of the diffraction data from the HIPPO 90° detectors for the extruded U–10Zr integrated for all detector panels at this diffraction angle into a single histogram for clarity. Backgrounds of patterns are subtracted. The diffraction patterns are obtained within the first 2 minutes at the given temperature. The sample has a Zr cladding extruded with the fuel alloy, therefore the peaks of α–Zr are also visible in the diffraction patterns. The full texture refinement, using data from individual detector panels rather than the full rings shown here and data from three sample rotations, was conducted on five phases, α–U, β–U, δ–UZr_2, γ–(U,Zr), and α–Zr.

At 200 and 600°C, peaks corresponding to α–U and δ–UZr_2 are distinct. On heating to 650°C, peaks for γ phase are present due to the phase transformation of δ–UZr_2 → γ–(U,Zr). The phase transformation of α–U → γ–(U,Zr) is completed at 670°C. The peaks of γ phase are present from 670°C heating to 650°C cooling. On cooling, the peaks of γ phase are gone at 600°C with the appearance of α–U and δ–UZr_2. Holding at 600°C during cooling, the diffraction peaks indicate the presence of α–U and δ–UZr_2, shown in Figure 3b.

The β–U phase peaks were not observed in the diffraction patterns. The β–U phase was refined in the refinement process using crystallographic parameters reported by Lawson et al. [23]. However, the peaks of β–U do not match with the measured diffraction pattern. The integrated diffraction pattern of all runs from 700°C to 650°C during cooling is shown in Figure 4. The diffraction pattern during heating exhibits similar characteristics. Therefore, β–U is determined to not occur at any temperature in the sample.

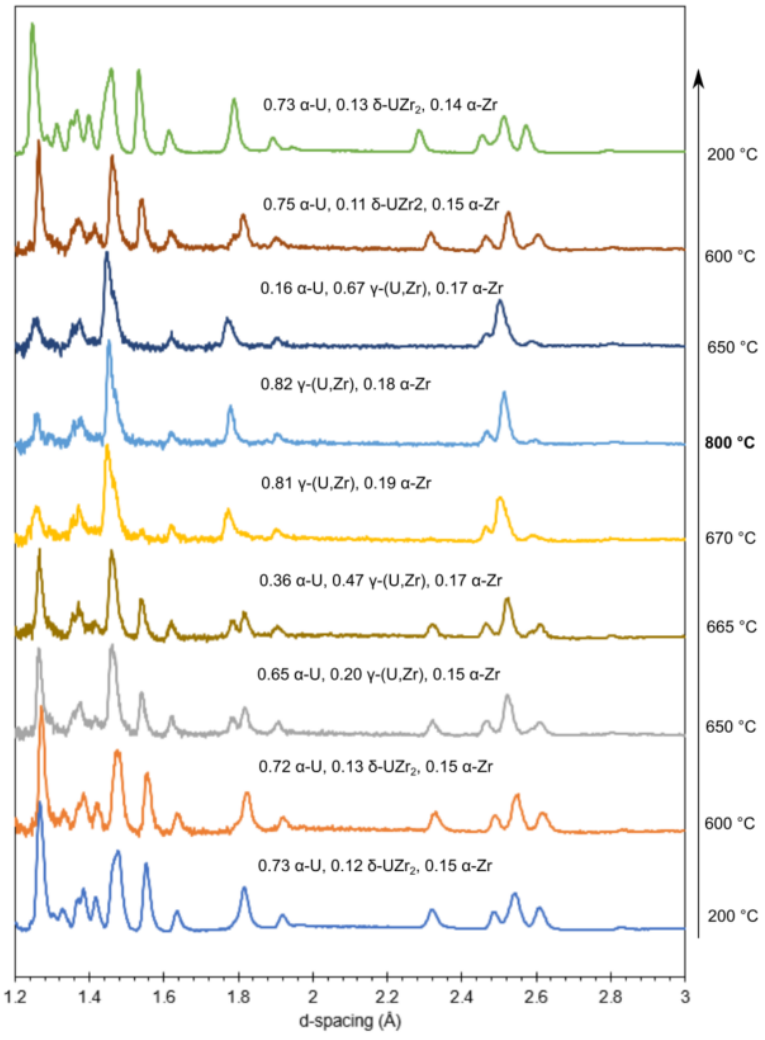

(a)

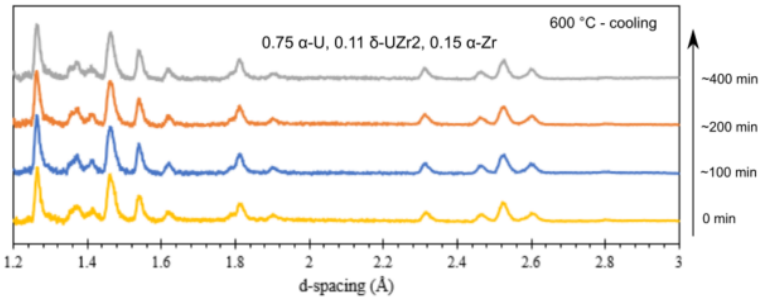

(b)

Figure 3. Diffraction patterns of the 90° detector bank (-45° sample rotation) with weight fractions of phases. (a) Obtained within the first 2 minutes at the given temperature, showing the disappearance of the α– and δ–phase reflections and appearance of γ–phase peaks during heating and the reverse during cooling. (b) Upon isothermal holding at 600°C during the cooling cycle.

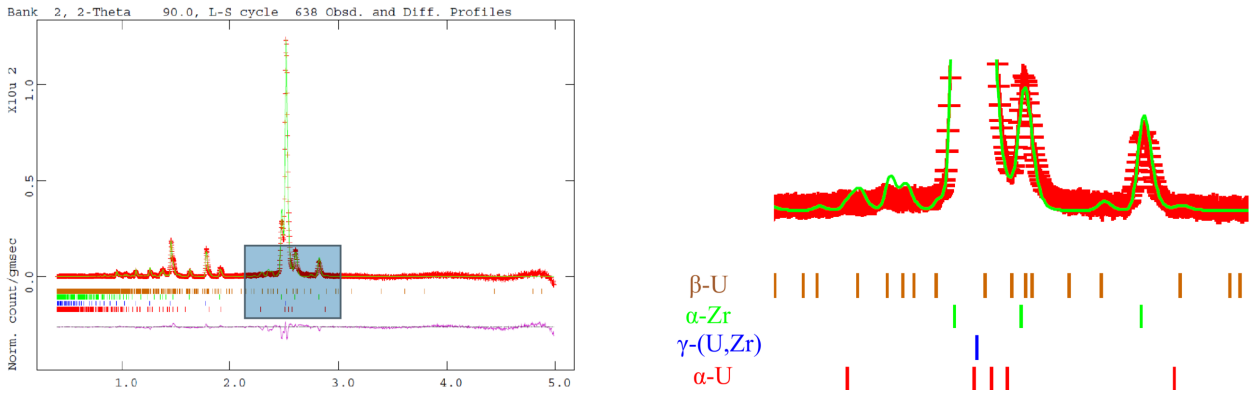

(a) (b)

Figure 4. (a) Diffraction pattern of all runs from 700°C to 650°C during cooling. (b) Magnification of the section of d-spacing in the highlighted region in (a), showing the peaks do not match with the reference peaks of β–U phase.

3.2. Weight fractions and lattice parameters

The weight fraction of Zr cladding and U–10Zr fuel in the sample from the Rietveld refinement varies between 0.14–0.19 and 0.81–0.86, respectively. The observed changes of the weight fraction of Zr cladding with temperature, which should be constant for a perfect refinement, is likely due to the U_{iso} parameter being constrained to be identical for all phases during refinement process. To be able to compare the results for the U–Zr phases with the phase diagram, the weight fractions of the phases in

U–10Zr are normalized to be 1, and the weight fractions of phases in the U–10Zr fuel, as discussed in the following, are after the normalization.

The weight fractions of phases during heating in the U–10Zr are shown in Figure 5. Below 600°C, the weight fractions are 86 wt. % α–U and 14 wt. % δ–UZr_2 consistently at all temperatures (Figure 5). Above 600°C, the γ phase weight fraction increases with temperature (Figure 5), increasing from ~ 0.57 at 665°C to 1.0 at 670°C when the α–U phase completely transforms to γ.

The lattice parameters of δ–UZr_2 increase with temperature, in the temperature range of 30–600°C, as listed in Table 1. The chemistry of the α–U and δ–UZr_2 is stable as the solubility of Zr in α–U is less than 1 at.% and Zr atoms reside in the δ–UZr_2 phase. Accordingly, the change of lattice parameter of δ–UZr_2 is a result of temperature rather than chemistry. By fitting the data of heating at 30°C–600°C, the temperature evolution of lattice parameters *a* and *c* are

(1)

(2)

where *a* and *c* are the lattice parameters in the unit of Å and T is the temperature in the unit of °C. The R–squared values are 0.9651 and 0.9394, respectively. Using a program for calculating the thermal expansion coefficient tensors (TEV [24]), the values of the temperature dependent thermal expansion coefficients are obtained as

(3)

Table 1. Evolution of lattice parameters of δ–UZr_2 during heating. The time is after the start of the experiment taken at the midpoint of the dataset.

Temperature (°C)	Time (min)	*a* (Å)	*c* (Å)
30	61	5.0427	3.0692
200	281	5.0483	3.0728
200	339	5.0469	3.0724
400	350	5.0634	3.0860
500	355	5.0638	3.0911
600	360	5.0789	3.0908

The lattice parameters *a* and *c*, for α–U, increase with temperature, while the parameter *b* decreases with temperature, shown in Figure 6a–c. Holding at 600°C during cooling, shown in Figure 6d–f, the parameters are stable over the observed period of ~540 min, and the lattice parameter values are same as at 600°C on heating. By fitting the data of heating at 30°C–665°C, the temperature evolution of lattice parameters *a*, *b*, and *c* are

(4)

(5)

(6)

where the lattice parameters are in the unit of Å and T is the temperature in the unit of °C. The R–squared values are 0.9988, 0.9627, 0.9934, respectively. The thermal expansion coefficient tensors for the entire temperature range are calculated by using the program TEV [24] and are listed in Eq. (7). The values are in good agreement to the data recommended by Touloukian et al. [10], with data listed in Table 2.

(7)

Table 2. Thermal expansion coefficients of lattice parameters of α–U recommended by Touloukian et al. [10].

T(°C)	*a*		*b*		*c*	
	linear expansion (%)	coefficient (/°C)	linear expansion (%)	coefficient (/°C)	linear expansion (%)	coefficient (/°C)
127	0.252	2.3551	0.002	0.018692	0.216	2.0187
227	0.511	2.4686	-0.018	-0.086957	0.451	2.1787
327	0.807	2.6287	-0.063	-0.20521	0.737	2.4007
427	1.161	2.8526	-0.162	-0.39803	1.09	2.6781
527	1.587	3.1302	-0.305	-0.60158	1.49	2.9389
627	2.104	3.4662	-0.452	-0.74465	1.907	3.1417
668	2.346	3.6204	-0.527	-0.81327	2.076	3.2037

The lattice parameter *a* of γ–(U,Zr) is shown in Figure 7. During heating, the parameter *a* decreases with temperature in the range of 650°C–670°C and increases with temperature at higher temperatures, indicating the effect of chemistry (i.e., U–Zr composition in γ). At 665°C, the parameter *a* decreases with time. The α–U phase disappears during the three runs collected at 670°C, where the weight fraction of γ jumps from 0.57 to 1.0, as mentioned above. During cooling, the lattice parameter decreases with temperature in the range of 800°C–650°C, however, the phase transformation of α–U was not observed up to this temperature during cooling. Only at 600°C was α–U observed again, indicating significant hysteresis. No splitting of peaks was observed during either heating or cooling at any of the temperatures investigated. Therefore, no evidence of two γ phases (i.e., γ_1 and γ_2) as indicated by the phase diagram was observed.

The lattice parameters of α–Zr are shown in Figure 8. By fitting the data of heating at 30°C–800°C, the temperature evolution of lattice parameters *a* and *c* are

(8)

(9)

where the lattice parameters are in the unit of Å and T is the temperature in the unit of °C. The R–squared values are 0.9834 and 0.963, separately. The thermal expansion coefficient tensors are listed in Eq. (10), which is very similar to the data recommended by Touloukian et al. [10], as listed in Table 3.

(10)

Table 3. Thermal expansion coefficients of lattice parameters of α–Zr recommended by Touloukian et al. [10].

T(°C)	*a*		*c*	
	linear expansion (%)	coefficient (/°C)	linear expansion (%)	coefficient (/°C)
127	0.051	0.47664	0.079	0.73832
227	0.102	0.49275	0.165	0.79710
327	0.156	0.50814	0.263	0.85668
427	0.212	0.52088	0.372	0.91400
527	0.269	0.53057	0.491	0.96844
627	0.325	0.53542	0.617	1.0165
727	0.382	0.54031	0.75	1.0608
827	0.436	0.54027	0.887	1.0991
864	0.455	0.53910	0.94	1.1137

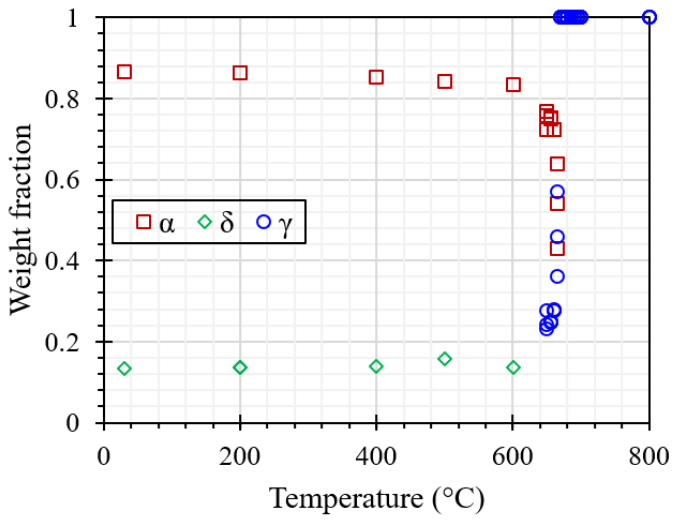

Figure 5. Temperature evolution of weight fraction of phases in the U–10Zr during heating.

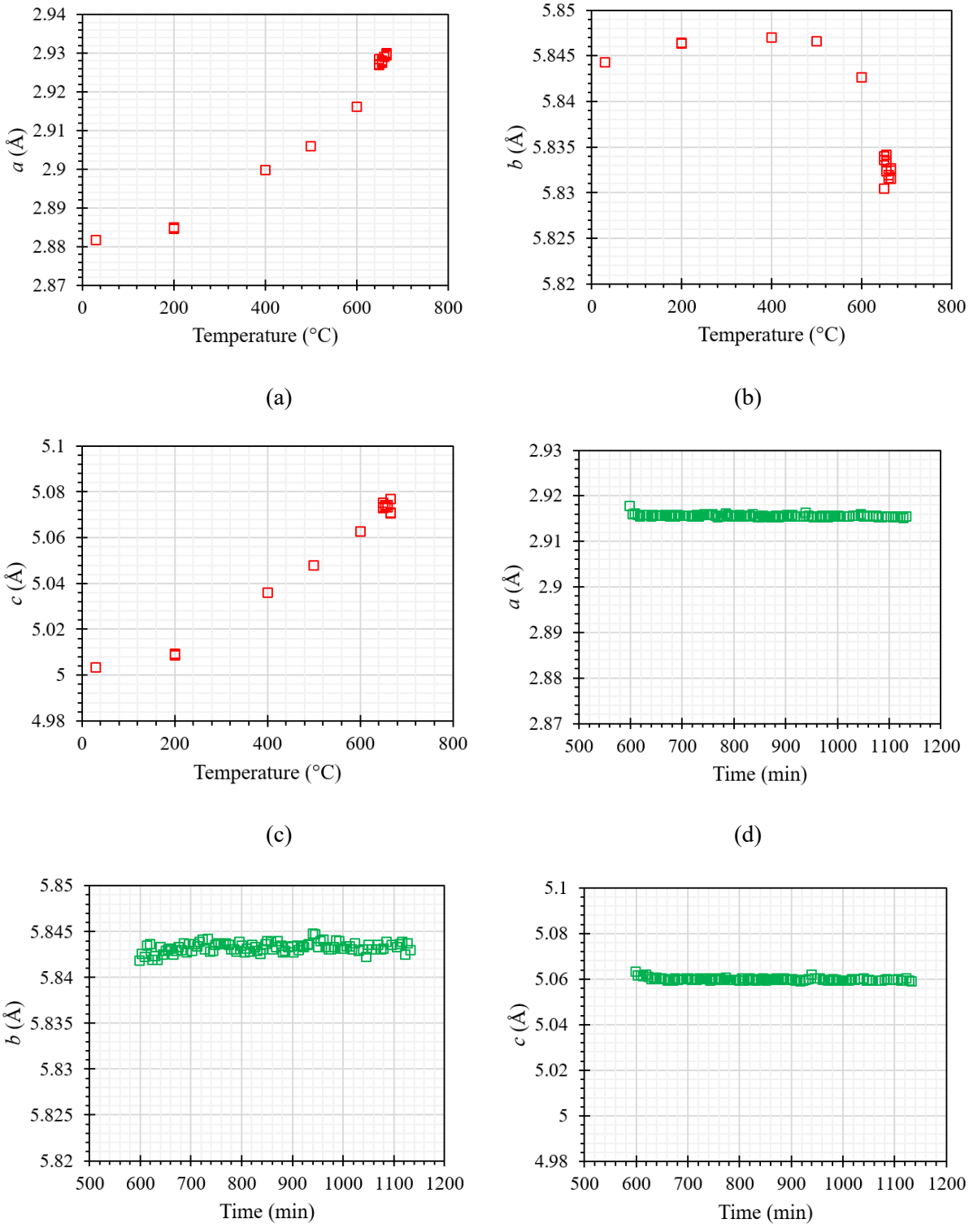

Figure 6. (a–c) Temperature evolution of lattice parameters of α–U during heating. (d–f) Time evolution of lattice parameters of α–U holding at 600°C.

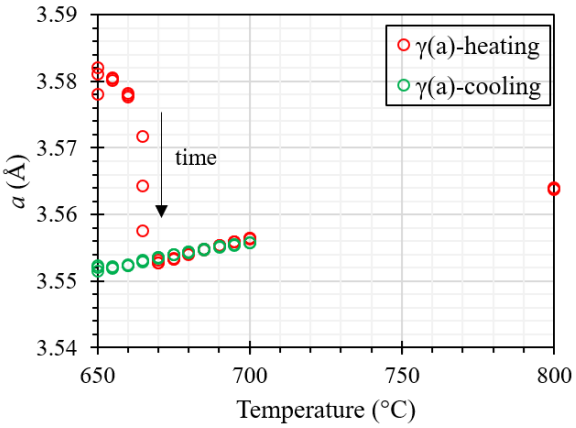

Figure 7. Temperature evolution of lattice parameter of γ–(U,Zr) during the thermal cycling. The arrow indicates the parameter evolves with time at the given temperature.

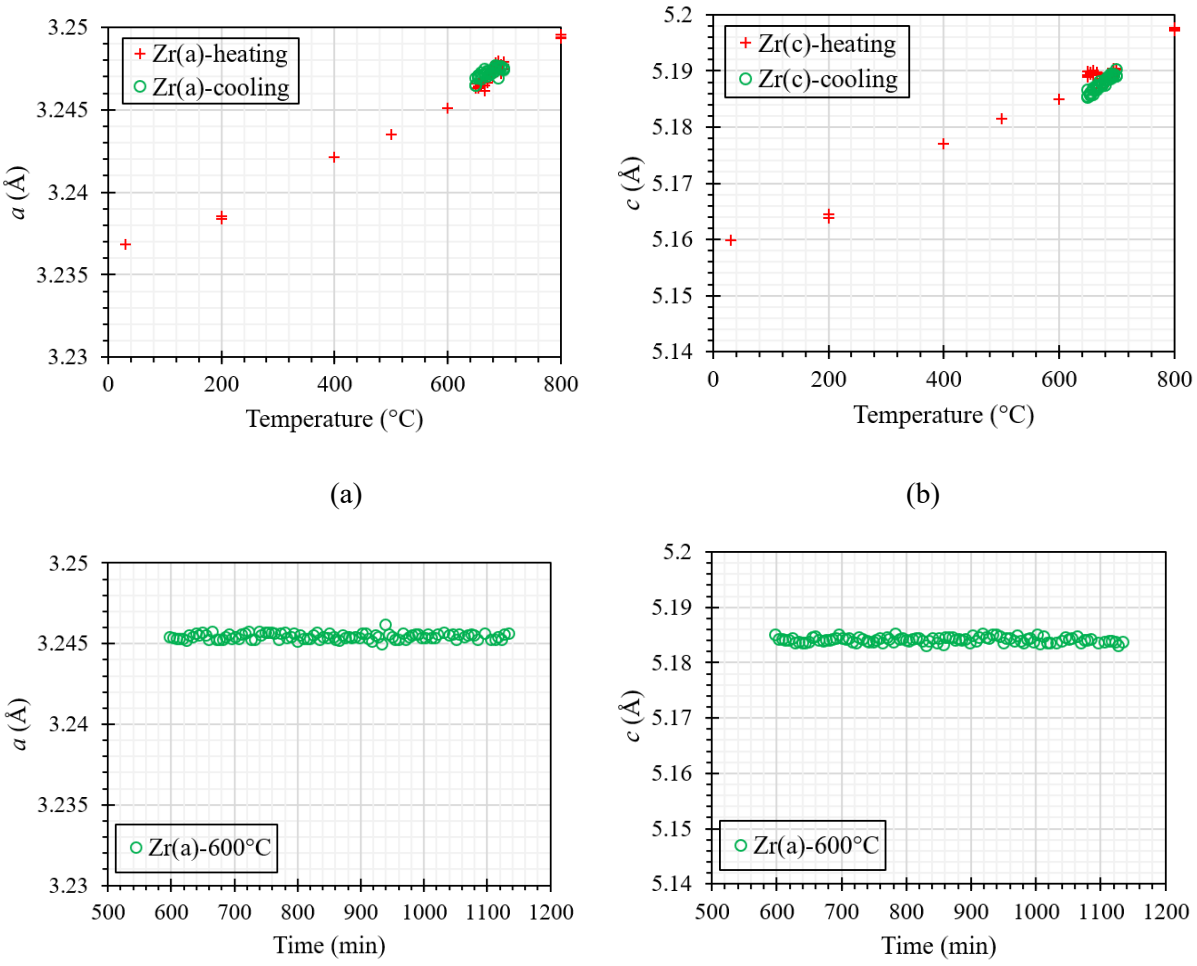

(c) (d)

Figure 8. (a–b) Temperature evolution of lattice parameters of α–Zr during thermal cycling. (c–d) Holding at 600°C during cooling.

3.3. Textures

The pole figures of α–U during thermal cycling are shown in Figure 9. As evidenced by the (200), (020), and (002) pole figures, the α–U phase has the c axis aligned with the extrusion direction in the center of the pole figures with the *a* and *b* axes correspondingly oriented radially to the extrusion direction. The maximum intensity in the $(001)_{\alpha}$ plane is constant during the thermal cycling as well as during holding at 600°C after the annealing at 800°C. The orientation distribution is therefore fully recovered after the annealing and not strengthening with temperature or time during the hold at 600°C.

The pole figures of δ–UZr_2 during heating are shown in Figure 10. The textures do not strengthen with temperature. The maximum texture, about 2.2 multiples of random distribution (MRD), is in the $(0001)_{\delta}$ and $(11\text{-}20)_{\delta}$ planes. The maximum texture in the $(0001)_{\delta}$ plane is not aligned parallel to the extrusion direction, rather along a radial direction. The maximum texture in the $(11\text{-}20)_{\delta}$ plane is aligned parallel to the extrusion direction. The $(20\text{-}20)_{\delta}$ pole figures exhibit textures roughly 1.5 MRD.

The pole figures of γ–(U,Zr) during the thermal cycling are shown in Figure 11. The pole figures for γ–(U,Zr) also show the fiber symmetry around the extrusion axis with the $(110)_{\gamma}$ lattice plane normal aligned parallel to the extrusion axis. The textures at 650°C and 665°C during heating are relatively weaker than the higher temperatures. Specifically, the maxima of the $(220)_{\gamma}$ pole figures strengthen from ~2.2 MRD to 2.7 MRD, and the maxima of the $(100)_{\gamma}$ pole figures increase from ~1.5 MRD to 2 MRD. Due to the orientation relationship between α–U and γ–(U,Zr) [25], pole figures of $(001)_{\alpha}$ and $(110)_{\gamma}$ show many similarities in terms of the position of the pole figure maxima. Since the multiplicity of the $(001)_{\alpha}$ is 2 and the multiplicity of the $(110)_{\gamma}$ is 12, one would expect a factor of 6 between the multiples of random distribution maxima above 1. We observe a maximum of ~5 MRD for $(001)_{\alpha}$, e.g. ~4 MRD above 1, which would translate to a maximum of ~4/6=0.66 above 1 or 1.66 MRD in $(110)_{\gamma}$.

The pole figures of α–Zr at all temperatures are shown in Figure 12. As expected for extruded Zr (e.g. [26]), a strong maximum of (10-10) exists along the extrusion direction. No changes were observed for the thermal cycling as the investigated temperatures are below the phase transformation temperature of Zr.

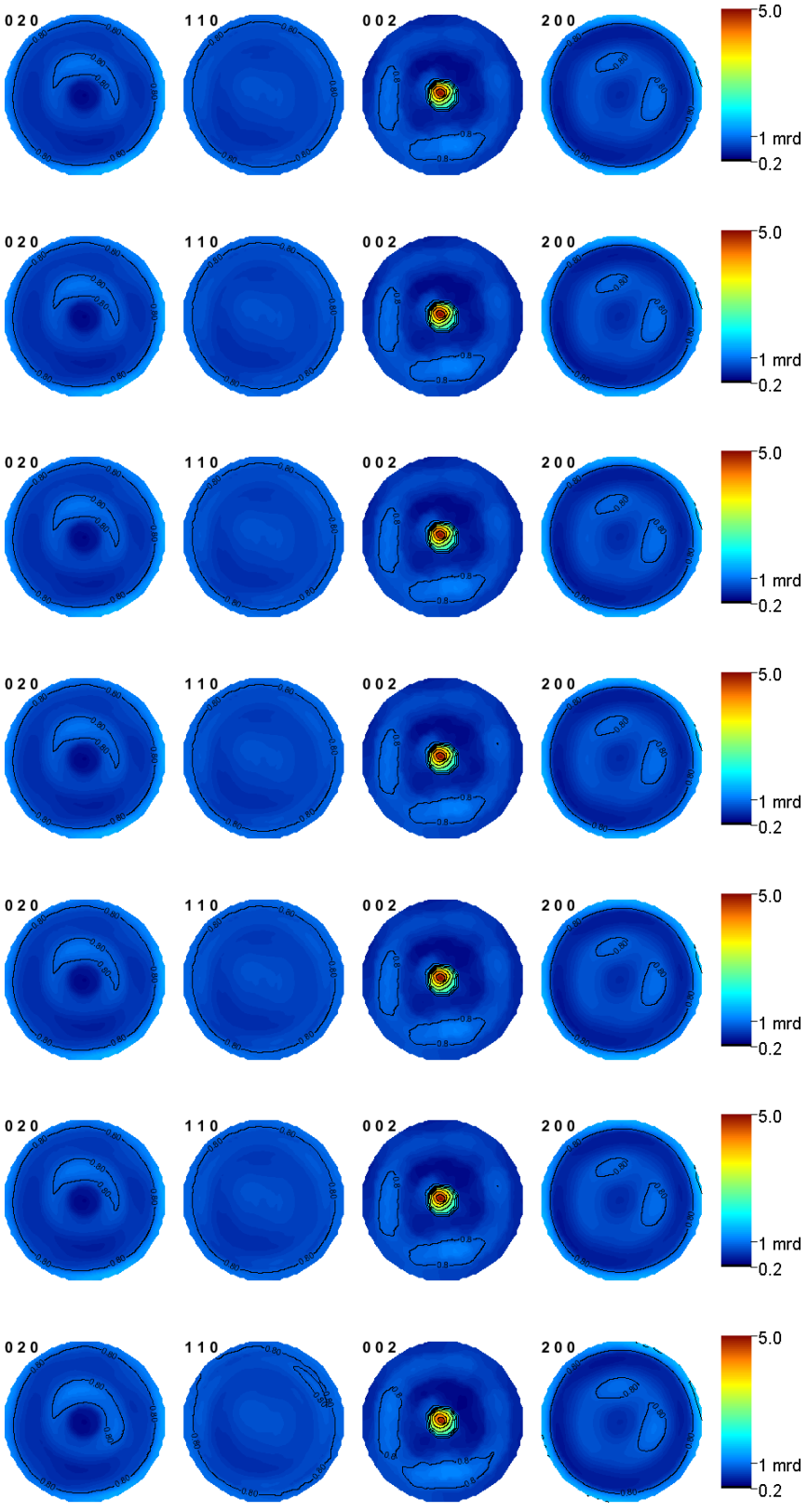

200Heat

600Heat

650Heat

665Heat

600Cool (0 min)

600Cool (400 min)

200Cool

Figure 9. Pole figures of α–U with temperature. The extrusion axis is in the center of the pole figures.

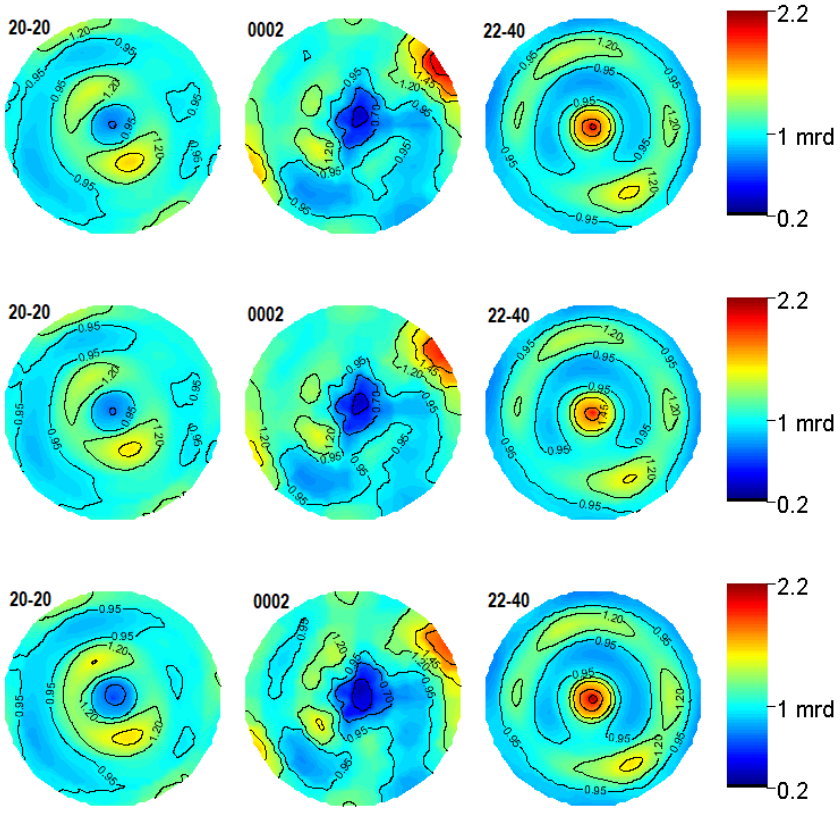

Figure 10. Pole figures of δ–UZr_2 with temperature.

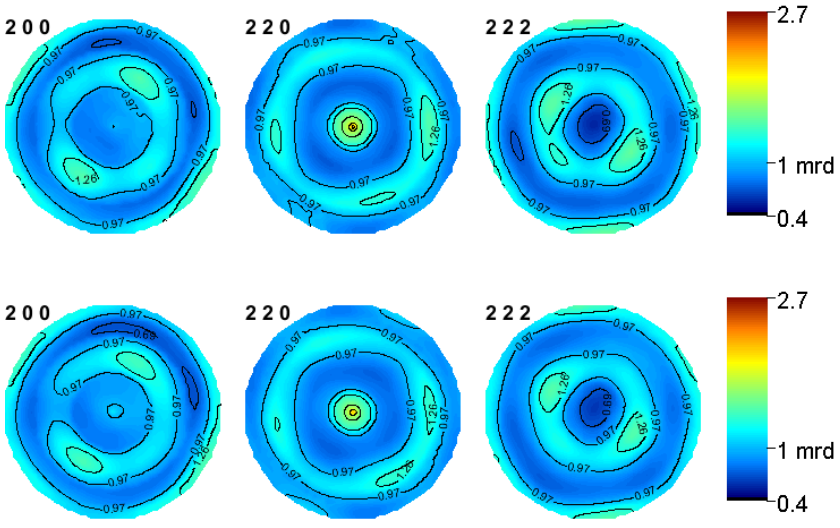

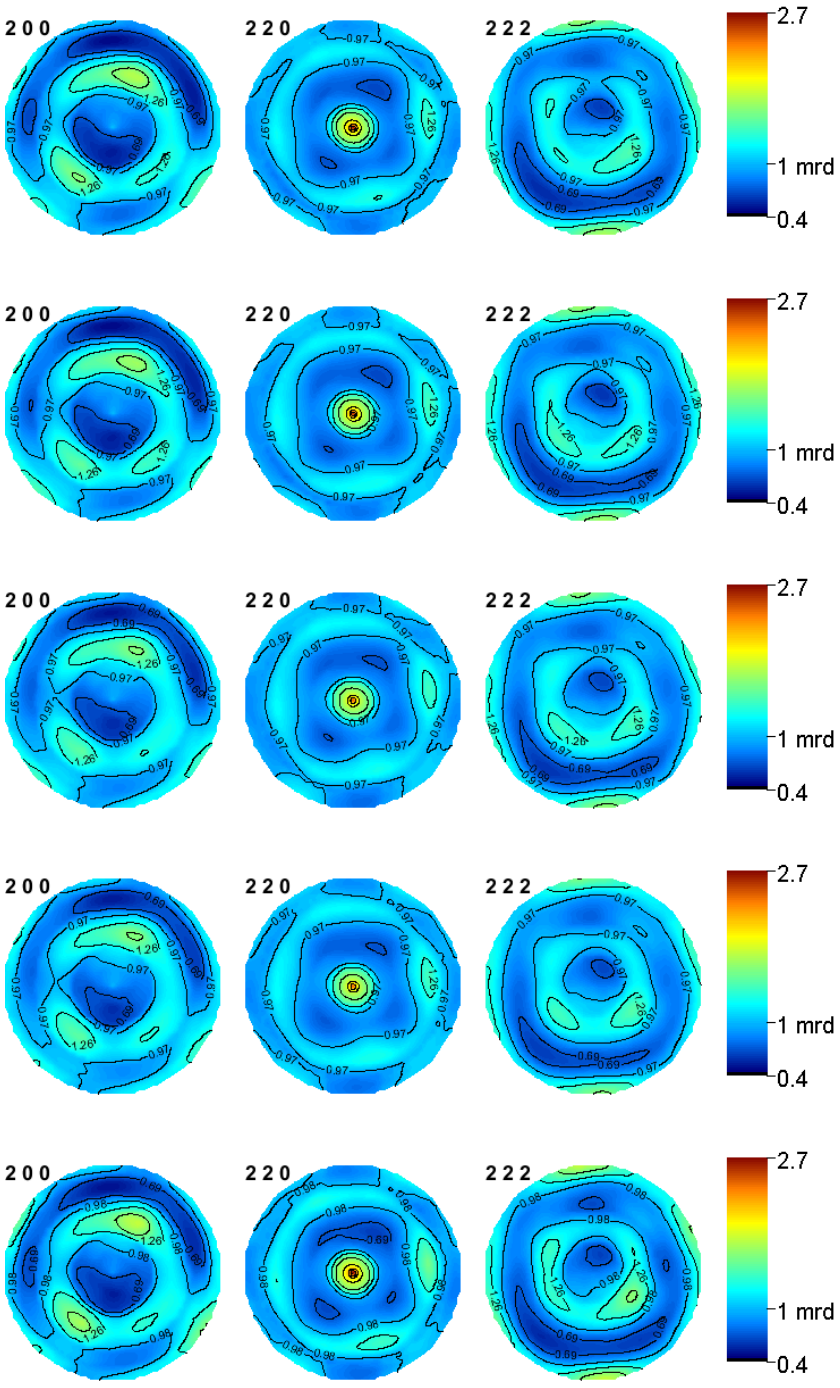

Figure 11. Pole figures of γ–(U,Zr) with temperature.

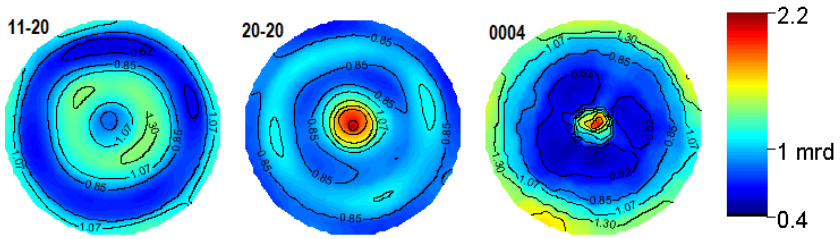

Figure 12. Pole figures of α–Zr at all temperatures.

4. Discussion

4.1. Hysteresis of phase transformation

The phase transformation of $\alpha + \gamma_2 \rightarrow \gamma$ was completed at 670°C during heating, and the reverse phase transformation occurred at a lower temperature, 650°C, which is indicated by the diffraction patterns shown in Figure 3a and weight fractions shown in Figure 5b. These behaviors are inconsistent with the equilibrium phase diagram as shown in Figure 1 [9], which shows that β–U transforms eutectoidally to α–U and γ_2–(U,Zr) at 662°C, and transforms to γ at 776°C. For the composition of U–10Zr wt. %, β–U transforms to γ_1–(U,Zr) at 693°C based on the phase diagram. The discrepancies between the measured data and the equilibrium phase diagram are greater on cooling than heating. This is not surprising, owing to the hysteresis encountered in the phase transformations. Due to the < 1 at. % solubility of Zr in α–U, formation of α–U during cooling, after the Zr atoms with an overall concentration of 22.5 at% were homogeneously distributed in the γ– (U,Zr) lattice during the annealing, requires significant repartitioning of Zr atoms during cooling for α–U to form. Therefore, equilibration and formation of α–U is sluggish, consistent with the low inter–diffusivity reported by others [27][28].

The β–U phase is absent in the diffraction patterns of the thermal cycling, and the result is consistent with the most recent in situ neutron diffraction study of as-cast U–10Zr alloy, though the sample was characterized after heating to 900°C in that study [29]. The diffraction peaks of the β–U phase during the thermal cycling have been observed in another study of a U–2wt. %Zr alloy, and the results will be reported in a separate manuscript. For the U–10Zr alloy, if considering the lever rule based on the U–Zr phase diagram, there should be a weight fraction of ~56-73 wt. % the β–U phase between 670-693°C, so the absence of β–U phase peaks is not because the fraction of the β–U phase is too low to be detected by the neutron diffraction technique. Whether the β–U phase exists in the U–10Zr alloy with longer hold times, as indicated by the phase diagram, needs to be further investigated especially using an in situ heating microstructural characterization technique. However, it is noteworthy that the phase diagram represents the equilibrium status, while the in situ heating technique captures the behavior of phase

transformation in a finite period of time.

4.2. Texture evolution

The material undergoes several phase transformations and because of that, changes in the observed textures before and after the maximum temperature could be expected. However, texture changes, such as moving from hoop to axial, were not observed. The intensity remains in the original orientation. Although some textures are relatively densified, the matrix texture is not strengthened during the thermal cycling, which indicates that the grains were not coarsening.

Preferred orientations are generated by the extrusion process. The preferred orientation, about 5 MRD, was observed in the $(100)_{\alpha}$ plane in the temperature range of 30–665°C during heating. These poles are aligned parallel to the extrusion direction. The texture components remain during the thermal cycling, which indicates absence of grain growth or preferential growth of favorably oriented grains. The maximum pole density in the $(001)_{\alpha}$ plane is greater than previously observed in the 600°C extruded U–10Zr alloy [15], which was ~ 2.5 MRD. This can be explained by the higher extrusion temperature of the U–10Zr used in this study (800°C). Moreover, in the present study, the maxima in the $(110)_{\alpha}$ planes were not observed; however, the previous study indicates textures, ~ 1.5 MRD, in the center of $(110)_{\alpha}$ planes.

At 650–665°C during heating, the $(110)_{\gamma}$ plane exhibits maxima along the extrusion direction, ~2.2 MRD. Since the α–U weight fraction remained approximately constant when the γ–(U,Zr) formed, the γ–(U,Zr) was transformed predominantly from δ–UZr_2 during heating. The previous study [15] indicates the orientation relationship $(111)_{\gamma}||(0001)_{\delta}$ with textures aligned along the extrusion direction in the 600°C extruded U–10Zr alloy. Basak et al. [30] also reported an orientation relationship $(111)_{\gamma}||(0001)_{\omega}$ and $<\text{-}110>_{\gamma}||<11\text{-}20>_{\omega}$. Indeed, the minimum observed in the $(0001)_{\delta}$ plane is reproduced in the $(111)_{\gamma}$. However, the ~2 MRD maximum at 2 o'clock in the (0001) plane of the δ–UZr_2 phase is not transferred to the (111) plane of the γ–(U,Zr) phase, indicating that this could possibly be an artefact of the texture analysis for a weak phase in the complex (i.e., orthorhombic α–U, hexagonal δ–UZr_2, and α–Zr) multi–phase system. On the other hand, the maxima observed in the $(11\text{-}20)_{\delta}$ plane is reproduced in the $(110)_{\gamma}$, though the relationship $(110)_{\gamma}||(11\text{-}20)_{\delta}$ was not reported before. Therefore, the texture of γ appears to be inherited from the δ–phase.

At and above 670°C, the texture in the γ–(U,Zr) phase, as evidenced by the $(220)_{\gamma}$ pole figure, strengthens, with the maximum along the extrusion direction increasing from 2.2 to 2.7 MRD. At these temperatures the γ phase originates both from δ–UZr_2 as well as from α–U, therefore, the γ shows a maximum in the $(220)_{\gamma}$ pole figure along the extrusion direction due to orientation relationships with both

the α and δ phases. Upon cooling, the maximum in the pole density is transferred again to the $(002)_\alpha$ poles, showing an almost perfect texture memory. The textures do not appear to undergo recrystallization by the nucleation of new crystals as no significant change in the strength of the pole density maxima is evident. This lack of recrystallization is clearly reflected in the texture of γ–(U,Zr) formed on heating, in which the pole figure of $(220)_\gamma$ directly maps to $(002)_\alpha$, which makes the textures in the α–U after the transformation cycling as strong as the initial. The study by Irukuvarghula et al. [15] indicates moderate textures of γ–(U,Zr) with intensity of 1.5 MRD in three planes, $(100)_\gamma$, $(110)_\gamma$ and $(111)_\gamma$, with textured cubic components in $(100)_\gamma$, center components in $(110)_\gamma$, and both center and cubic components in $(111)_\gamma$. Although the present study indicates these textured components in the three planes, the maximum intensity is in the $(110)_\gamma$ plane only, while the $(100)_\gamma$ and $(111)_\gamma$ planes do not exhibit the same strong texture as $(110)_\gamma$.

The maximum texture of both planes, $(001)_\alpha$ and $(110)_\gamma$, during the thermal cycling are aligned parallel to the extrusion direction, indicating the inheritance of textures between the two phases. The $(110)_\gamma$ has a multiplicity of 12 and the $(001)_\alpha$ has a multiplicity of 2. Each of the six $(110)_\gamma$ axes could become a $(001)_\alpha$ axis, but the material selects the one that is aligned parallel to the extrusion direction, which indicates variant selection between $(001)_\alpha$ and $(110)_\gamma$ must be occurring (see e.g. Tomida [31] for discussion of different variant selection mechanisms and models in steel). Without variant selection, the texture would likely be considerably randomized by the phase transformation. Such a variant selection of the orthorhombic phase with the BCC parent phase has been revealed previously in the Ti–Al–Nb–based alloys [32] [33]. The orientation relationship is $\{001\}_{\text{orthorhombic}} || \{110\}_{\text{BCC}}$. The specific orientation relationship $\{001\}_\alpha || \{110\}_\gamma$ was observed in this study, in which α is orthorhombic structure, and γ is BCC structure. The previous study [15] on the 600°C extruded U–10Zr alloy, however, did not find the variant selection between α and γ.

The texture intensity in both α–U and γ–(U,Zr) of the U-10Zr in this investigation, extruded at 800°C, are stronger than the 600°C extruded U-10Zr reported by Irukuvarghula et al. [15]. The alloy at higher temperature is softer than at the lower temperature, making the extrusion deformation easier to develop. The higher extrusion temperature accelerates growth of crystals and generation of more deformation–introduced dislocations compared to the lower temperature. The surrounding grains that have a slightly stiffer direction pushing on the grain transform, resulting in the variant selection observed between α and γ. A detailed analysis of the active variant selection mechanism requires modeling and is beyond the scope of this study.

5. Conclusion

This study establishes a fundamental understanding of the processes prevailing in the 800°C extruded U–10Zr system during thermal cycling. The following conclusions can be drawn from the data presented:

- Heating and cooling substantially changed the microstructure with respect to crystallographic texture, phase composition, and lattice parameters. Lattice parameters as well as the thermal expansion coefficients of α–U, δ–UZr_2, and α–Zr at different temperatures during the thermal cycling are obtained. The α–U phase exhibits lattice contraction with increasing temperature along the *b* lattice direction and lattice expansion in the other directions while the other phases exhibit lattice expansion with temperature in all directions.
- The in situ heating neutron diffraction indicates the phase transformation of γ–(U,Zr) → α–U + γ_2 during cooling is slower than the reverse transformation during heating. This hysteresis of the phase transformation can be explained by sluggish repartitioning of Zr atoms to form virtually Zr-free volume for the formation of α-U.
- The β–U phase is absent at the temperatures, heating rates, and holding times of the thermal cycling of this experiment, which differs from the equilibrium U–Zr phase diagram. The study indicates that further investigation of the U-rich region in the U–Zr phase diagram is needed to improve the understanding and description of the U–Zr system.
- The sample exhibits strong textures with $(001)_\alpha$ and $(110)_\gamma$ planes aligned parallel to the extrusion direction. The maximum pole density of α–U is in the $(001)_\alpha$ plane and the intensity is ~ 5 MRD. The maximum pole density of γ–(U,Zr) is in the $(110)_\gamma$ plane and the intensity is ~ 2.7 MRD. This texture is stronger than those observed for the U-10Zr extruded at a lower temperature (600°C) in the literature [15]. Compared to the lower extrusion temperature, the higher extrusion temperature applied to the material studied here likely accelerated growth of crystals and due to easier generation of more dislocations lead to a larger amount of crystal reorientation. The variant selection of $(001)_\alpha \| (110)_\gamma$ is observed while not reported previously.

Acknowledgments

This work was supported by the US Department of Energy, Office of Nuclear Energy under DOE Idaho Operations Office Contract DE–AC07–05ID14517, and UT–Battelle, LLC, under contract DE–AC05–00OR22725. Accordingly, the US Government retains and the publisher, by accepting the article for publication, acknowledges that the US Government retains a nonexclusive, paid–up, irrevocable, worldwide license to publish or reproduce the published form of this manuscript or allow

others to do so, for US Government purposes. DOE will provide public access to these results of federally sponsored research in accordance with the DOE Public Access Plan (http://energy.gov/downloads/doe–public–access–plan). The work has benefitted from the use of the Los Alamos Neutron Science Center (LANSCE) at Los Alamos National Laboratory. Los Alamos National Laboratory is operated by Triad National Security, LLC, for the National Nuclear Security Administration of the U.S. Department of Energy under contract number 89233218NCA000001.

US Department of Energy Disclaimer

References

[1] D.E. Janney, S.L. Hayes, Experimentally Known Properties of U-10Zr Alloys: A Critical Review, Nucl. Technol. 203 (2018) 109–128. https://doi.org/10.1080/00295450.2018.1435137.

[2] L.C. Walters, Thirty years of fuels and materials information from EBR-II, J. Nucl. Mater. 270 (1999) 39–48. https://doi.org/10.1016/S0022-3115(98)00760-0.

[3] D.C. Crawford, D.L. Porter, S.L. Hayes, Fuels for sodium-cooled fast reactors: US perspective, J. Nucl. Mater. 371 (2007) 202–231. https://doi.org/10.1016/J.JNUCMAT.2007.05.010.

[4] D.E. Janney, Metallic fuels handbook, Part 1: alloys based on U-Zr, Pu-Zr, U-Pu, or U-Pu-Zr, including those with minor actinides (Np, Am, Cm), rare-earth elements (La, Ce, Pr, Nd, Gd), and Y (INL/EXT-15-36520), Idaho Falls, ID, 2018.

[5] D.E. Janney, S.L. Hayes, C.A. Adkins, A Critical Review of the Experimentally Known Properties of U-Pu-Zr Alloys. Part 2: Thermal and Mechanical Properties, Nucl. Technol. 206 (2020) 1–22. https://doi.org/10.1080/00295450.2019.1623617.

[6] D.E. Janney, S.L. Hayes, C.A. Adkins, A Critical Review of the Experimentally Known Properties of U-Pu-Zr Alloys. Part 1: Phases and Phase Diagrams, Nucl. Technol. 205 (2019) 1387–1415. https://doi.org/10.1080/00295450.2019.1578573.

[7] C.W. Wilkes, G.L. Batte, D.B. Tracy, V. Griffiths, EBR-II fuel slug casting experience (ANL-IFR-73), Idaho Falls, ID, 1987.
[8] D. Pace, B. Mackowiak, Extrusion development report (INL/EXT-18-44551), Idaho Falls, ID, 2018.
[9] R.I. Sheldon, D.E. Peterson, The U-Zr (Uranium-Zirconium) system, Bull. Alloy Phase Diagrams. 10 (1989) 165–171. https://doi.org/10.1007/BF02881432.
[10] Y.S. Touloukian, R.K. Kirby, R.E. Taylor, P.D. Desai, Thermophysical properties of matter - the TPRC data series. Volume 12. Thermal expansion metallic elements and alloys, West Lafayette, IN, 1975.
[11] T.J. Barrett, R.J. McCabe, D.W. Brown, B. Clausen, S.C. Vogel, M. Knezevic, Predicting deformation behavior of α-uranium during tension, compression, load reversal, rolling, and sheet forming using elasto-plastic, multi-level crystal plasticity coupled with finite elements, J. Mech. Phys. Solids. 138 (2020) 103924. https://doi.org/10.1016/j.jmps.2020.103924.
[12] R.W. Cahn, Plastic deformation of alpha-uranium: twinning and slip, Acta Metall. 1 (1953) 49–70. https://doi.org/10.1016/0001-6160(53)90009-1.
[13] R.J. McCabe, L. Capolungo, P.E. Marshall, C.M. Cady, C.N. Tomé, Deformation of wrought uranium: Experiments and modeling, Acta Mater. 58 (2010) 5447–5459. https://doi.org/10.1016/J.ACTAMAT.2010.06.021.
[14] G.L. Hofman, S.L. Hayes, M.C. Petri, Temperature gradient driven constituent redistribution in U-Zr alloys, J. Nucl. Mater. 227 (1996) 277–286. https://doi.org/10.1016/0022-3115(95)00129-8.
[15] S. Irukuvarghula, B. Blamer, S. Ahn, S.C. Vogel, A.S. Losko, S.M. McDeavitt, Texture evolution during annealing of hot extruded U-10wt%Zr alloy by in situ neutron diffraction, J. Nucl. Mater. 497 (2017) 10–15. https://doi.org/10.1016/J.JNUCMAT.2017.09.008.
[16] M. Knezevic, L. Capolungo, C.N. Tomé, R.A. Lebensohn, D.J. Alexander, B. Mihaila, R.J. McCabe, Anisotropic stress–strain response and microstructure evolution of textured alpha-uranium, Acta Mater. 60 (2012) 702–715. https://doi.org/10.1016/j.actamat.2011.10.041.
[17] S.C. Vogel, S. Takajo, M.A. Kumar, E.N. Caspi, A. Pesach, E. Tiferet, O. Yeheskel, Ambient and high-temperature bulk characterization of additively manufactured Ti-6Al-4V using neutron diffraction, JOM. 70 (2018) 1714–1722. https://doi.org/10.1007/s11837-018-3038-2.
[18] H.-R. Wenk, L. Lutterotti, S. Vogel, Texture analysis with the new HIPPO TOF diffractometer, Nucl. Instruments Methods Phys. Res. Sect. A Accel. Spectrometers, Detect. Assoc. Equip. 515 (2003) 575–588. https://doi.org/10.1016/j.nima.2003.05.001.
[19] S. Takajo, S.C. Vogel, Determination of pole figure coverage for texture measurements with neutron time-of-flight diffractometers, J. Appl. Crystallogr. 51 (2018) 895–900.

[20] H.-R. Wenk, L. Lutterotti, S.C. Vogel, Rietveld texture analysis from TOF neutron diffraction data, Powder Diffr. 25 (2010) 283–296. https://doi.org/10.1154/1.3479004.
[21] A.C. Larson, R.B. Von Dreele, General structure analysis sytem (GSAS) LAUR 86-748, Los Alamos, NM, 1994.
[22] S.C. Vogel, Gsaslanguage: A GSAS script language for automated Rietveld refinements of diffraction data, J. Appl. Crystallogr. 44 (2011) 873–877. https://doi.org/10.1107/S0021889811023181.
[23] A.C. Lawson, C.E. Olsen, J.W. Richardson, M.H. Mueller, G.H. Lander, Structure of β-uranium, Acta Crystallogr. Sect. B Struct. Sci. 44 (1988) 89–96. https://doi.org/10.1107/S0108768187009406.
[24] T. Langreiter, V. Kahlenberg, TEV – a program for the determination and visualization of the thermal expansion tensor from diffraction data, Crystals. 5 (2015) 143–153. https://doi.org/10.3390/cryst5010143.
[25] B.A. Hatt, The orientation relationship between the gamma and alpha structures in uranium-zirconium alloys, J. Nucl. Mater. 19 (1966) 133–141. https://doi.org/10.1016/0022-3115(66)90102-4.
[26] M.R. Daymond, R.A. Holt, S. Cai, P. Mosbrucker, S.C. Vogel, Texture inheritance and variant selection through an hcp-bcc-hcp phase transformation, Acta Mater. 58 (2010) 4053–4066. https://doi.org/10.1016/j.actamat.2010.03.012.
[27] T. Ogata, M. Akabori, A. Itoh, T. Ogawa, Interdiffusion in uranium-zirconium solid solutions, J. Nucl. Mater. 232 (1996) 125–130. https://doi.org/10.1016/S0022-3115(96)00409-6.
[28] C.B. Basak, Microstructural evaluation of U-rich U-Zr alloys under near-equilibrium condition, J. Nucl. Mater. 416 (2011) 280–287. https://doi.org/10.1016/j.jnucmat.2011.06.011.
[29] W.J. Williams, M.A. Okuniewski, S.C. Vogel, J. Zhang, In Situ Neutron Diffraction Study of Crystallographic Evolution and Thermal Expansion Coefficients in U-22.5 at.%Zr During Annealing, JOM. 72 (2020) 2042–2050. https://doi.org/10.1007/s11837-020-04086-8.
[30] C.B. Basak, S. Neogy, D. Srivastava, G.K. Dey, S. Banerjee, Disordered bcc γ-phase to δ-phase transformation in Zr-rich U-Zr alloy, Philos. Mag. 91 (2011) 3290–3306. https://doi.org/10.1080/14786435.2011.577756.
[31] T. Tomida, Variant selection mechanism by elastic anisotropy and double K-S relation for transformation texture in steel; difference between martensite and ferrite, Acta Mater. 146 (2018) 25–41. https://doi.org/10.1016/j.actamat.2017.12.033.
[32] Y. Zheng, W. Zeng, D. Li, J. Xu, X. Ma, X. Liang, J. Zhang, Orthorhombic precipitate variant selection in a Ti2AlNb based alloy, Mater. Des. 158 (2018) 46–61. https://doi.org/10.1016/j.matdes.2018.08.011.

[33] C.J. Boehlert, B.S. Majumdar, V. Seetharaman, D.B. Miracle, Part I. The microstructural evolution in Ti-Al-Nb O + Bcc orthorhombic alloys, Met. Mater. Trans. A. 30 (1999) 2305–2323. https://doi.org/10.1007/s11661-999-0240-4.